1 **Patterns of Alluviation in Mixed Bedrock-Alluvial Channels: 1. Numerical Model**

2 **Jongseok Cho[1] and Peter A. Nelson[1]**

3 [1]Department of Civil and Environmental Engineering, Colorado State University, Fort Collins,

4 Colorado, USA.

5 Corresponding author: Peter Nelson (peter.nelson@colostate.edu)

6 **Key Points:**

7 • A new model is developed to predict the dynamics of alluvial patterns in mixed bedrock-

8 alluvial channels.

9 • The model accurately predicts bedform evolution in an alluvial channel and alluvial patch

10 formation in a mixed bedrock-alluvial channel.

11 • Accounting for differential roughness and shear stress correction are important for model

12 prediction of the degree of exposed bedrock.

13

14 **Abstract**

15 Mixed bedrock-alluvial rivers can exhibit partial alluvial cover, which may play an important

16 role in controlling bedrock erosion rates and landscape evolution. However, numerical

17 morphodynamic models generally are unable to predict the pattern of alluviation in these

18 channels. Hence we present a new two-dimensional depth-averaged morphodynamic model that

19 can be applied to both fully alluvial and mixed bedrock-alluvial channels, and we use the model

20 to gain insight into the mechanisms responsible for the development of sediment patches and

21 patterns of bedrock alluviation. The model computes hydrodynamics, sediment transport, and

22 bed evolution, using a roughness partitioning that accounts for differential roughness of sediment

23 and bedrock, roughness due to sediment transport, and form drag. The model successfully

24 replicates observations of bar development and migration from a fully alluvial flume experiment,

25 and it models persistent sediment patches observed in a mixed bedrock-alluvial flume

26 experiment. Numerical experiments in which the form drag, sediment transport roughness, and

27 ripple factor correction were neglected did not successfully reproduce the observed persistent

28 sediment cover in the mixed bedrock-alluvial case, suggesting that accounting for these different

29 roughness components is critical to successfully model sediment dynamics in bedrock channels.

30 **Plain Language Summary**

31 The spatial distribution of sediment patches in bedrock rivers can play an important role in the

32 local hydraulic conditions as well as long-term channel and landscape evolution, because

33 sediment in these channels is an important mechanism of bedrock erosion. Flume experiments

34 and field studies have shown that the amount of sediment cover and the pattern of sediment

35 patches in these streams can sometimes reach a sort of equilibrium, but numerical models have

36 been largely unable to replicate those observations. Here, we present a new numerical model for

37 mixed bedrock-alluvial rivers that explicitly accounts for different roughness feedbacks between

38 the bedrock, sediment, and flow field. We show that the model can successfully simulate

39 observations from flume experiments conducted with and without exposed bedrock, and it is able

40 to simulate persistent partial sediment cover. These conditions develop because of the

41 complicated roughness feedbacks in these channels, which we demonstrate through simulations

42 where different roughness components are "turned off," which result in completely exposed

43 bedrock without sediment cover.

44 **1 Introduction**

45 River channels can be classified as either alluvial, bedrock, or mixed bedrock-alluvial

46 (Howard, 1980, 1987, 1998; Howard et al., 1994; Knighton, 2014). The beds of alluvial rivers

47 are entirely covered by sediment of sufficient thickness so that the underlying bedrock is not

48 exposed (Tinkler & Wohl, 1998; Whipple, 2004). In contrast, bedrock channels are characterized

49 by frequently exposed bedrock and a lack of continuous alluvial cover in the channel bed and

50 banks. Mixed bedrock-alluvial channels tend to have sediment supply that is less than their

51 sediment transport capacity, and they feature the exposed bedrock interspersed with patches of

52 alluvial cover, potentially taking the form of alternate bars (e.g., Chatanantavet & Parker, 2008)

53 or point bars at meander bends (P. A. Nelson et al., 2014; Nittrouer et al., 2011).

54 The pattern of alluvial cover in mixed bedrock-alluvial channels likely plays a role in the

55 morphological evolution of those channels, and consequently on landscape evolution (Gasparini

56 et al., 2007; Hodge & Hoey, 2012; Howard et al., 1994; Seidl & Dietrich, 1992; Tinkler & Wohl,

57 1998; Whipple & Tucker, 2002; Wohl, 1993). Bedrock channel erosion sets the lower boundary

58 condition for landscape evolution and bedrock channels convey climatic and tectonic

59 perturbation through the landscape (Whipple, 2001; Whipple & Tucker, 1999). Alluvial cover is

60   an important component of mechanistic models of bedrock erosion; for example, the saltation-

61   abrasion model incorporates the erosional mechanism of saltating bedload particles impacting

62   and eroding bedrock (Demeter et al., 2005; Hartshorn et al., 2002; Sklar & Dietrich, 1998, 2001,

63   2004; Zhang et al., 2015). Competition between the tools and cover effects controls the spatial

64   distribution of the bedrock channel erosion that results in lateral and vertical channel erosion and

65   meandering (Finnegan et al., 2007; Lamb et al., 2015; Turowski et al., 2007; Turowski, Hovius,

66   Meng-Long, et al., 2008; Turowski, Hovius, Wilson, et al., 2008).

67   Observations from flume experiments documenting the development of alluvial cover

68   patterns on bedrock beds have shown that alluvial cover in these channels depends on channel

69   slope, the initial thickness of alluvial sediment, sediment supply, bedrock roughness, and channel

70   topography. Chatanantavet and Parker (2008) conducted a series of experiments in a straight

71   flume where they varied the rate of sediment supply, the initial cover of sediment on the bed, the

72   slope, and the grain size. Their experiments illuminated several exciting phenomena in mixed

73   bedrock-alluvial channels. First, the pattern and trajectory of the alluvial cover appear to be

74   slope-dependent, wherein at low slopes ($S = 0.0115$) the exposed bed fraction linearly decreases

75   with increasing sediment supply, akin to the linear relationship hypothesized by Sklar and

76   Dietrich (2004). However, at higher slopes ($S = 0.02$), experiments starting with a bare bed did

77   not develop persistent alluvial cover at any supplied rate until that rate exceeded the overall

78   transport capacity of the channel. At that point, "runaway alluviation" occurred, and the entire

79   channel became covered in sediment. Second, the thickness of the initial alluvial cover affected

80   the dynamics of alluviation on the bed, wherein at low initial alluvial thickness the bed was

81   stripped clean, whereas thicker initial sediment covers eventually reached a non-zero fraction of

82   bedrock exposure. Third, some of their experiments developed continuous strips of sediment

83   moving from one side of the channel to the other, akin to alternate bars.

84   Other experiments have suggested that bedrock topography and the relative hydraulic

85   roughness of bedrock relative to grain size plays a role in alluvial dynamics of mixed bedrock-

86   alluvial channels. Mishra and Inoue (2020) performed flume experiments with varying bedrock

87   roughness. The observed the extent of alluvial cover increases with increasing sediment supply

88   when the hydraulic roughness of the bedrock bed is larger than that of the alluvial surface.

89   However, a sudden transition from bare bedrock bed to full alluviation was observed as sediment

90   supply momentarily exceeded the channel's transport capacity when the ratio of hydraulic

91   roughness height of bedrock to grain size (k_{sb}/d) is 1.9 or lower. They also proposed an

92   approximation of dimensionless critical shear stress for incipient particle motion over bedrock

93   beds as a function of relative roughness height. Hodge and Hoey (2016a, 2016b) performed

94   experiments in a 3D printed scale model of a jointed limestone bedrock river in which the

95   patterns of sediment deposits at different sediment supply rates were documented. Their

96   experiments pointed out the importance of bedrock topography on depositional patterns, as

97   patches of sediment tended to form in the lowest portions of the bed, and at higher discharge and

98   sediment supply, the bed topography played a less important role than sediment-sediment and

99   sediment-flow interactions in stabilizing patches of alluvium.

100   Numerical models of sediment transport and bed evolution in mixed bedrock-alluvial

101   channels have struggled to capture the dynamics of alluvial cover observed in experiments or in

102   the field. Morphodynamic models simulate river channel evolution by iteratively using hydraulic

103   flow field calculations to estimate sediment transport rates, which are then used in the

104   conservation of sediment mass (i.e., the Exner equation) to calculate bed erosion and deposition

105   patterns. These types of models have been used for decades to understand the dynamics of

106   alluvial rivers, such as the development and migration of alternate bars (e.g., Bernini et al., 2006;

107   Defina, 2003; Qian et al., 2017), sediment sorting (e.g., P. A. Nelson et al., 2015a, 2015b),

108   braiding (e.g., Murray & Paola, 1997; Schuurman et al., 2013), meandering (e.g., Smith &

109   Mclean, 1984; J. M. Nelson et al., 2003), and armoring (e.g., Parker & Klingeman, 1982; Parker

110   & Toro-Escobar, 2002). However, alluvial morphodynamic models generally assume that the

111   sediment supply equals or exceeds the sediment transport capacity, which is not the case for

112   mixed bedrock-alluvial rivers.

113   This assumption has only recently begun to be relaxed in attempts to use morphodynamic

114   models to better understand mixed bedrock-alluvial rivers (e.g., P. A. Nelson & Seminara, 2012).

115   Using a cellular automaton model governed by probabilities of individual grain movement,

116   Hodge and Hoey (2012) studied the relationship between the fraction of bedrock exposure and

117   the ratio of sediment supply to capacity on noneroding bedrock beds. Zhang et al. (2015)

118   expressed bedrock cover fraction as a ratio of vertical length scale between alluvial thickness and

119   macro-roughness of bedrock topography representing the statistical characteristics of bedrock

120   surface fluctuations. This MRSAA (Macro-Roughness-based Saltation-Abrasion-Alluviation)

121   model was later implemented to investigate the knickpoint migration (Zhang et al., 2018, 2019)

122   and formation of the cyclic steps (Izumi et al., 2017) to spatiotemporal variation of sediment

123   supply. Inoue et al. (2016) provided an early attempt to investigate alternate bar formation and

124   bedrock incision in mixed bedrock-alluvial channels in response to the different ratio of sediment

125   supply to channel's transport capacity.

126   Larger-than-grain-scale bedrock topography, sometimes called "macrotopography", has

127   recently been incorporated into one-dimensional morphodynamic models (Zhang et al., 2015).

128   The model solutions for alluvial response to sediment supply show that stripping of antecedent

129   sediment from upstream to downstream occurs with the termination of sediment supply, and the

130   development of an alluvial layer with a thickness corresponding to the ratio of sediment supply

131   to transport capacity (q_s / q_c), which propagates downstream over bare bedrock when the

132   sediment supply is increased. Application of nonlinear wave speed to the alluvial layer predicted

133   that alluvium over a bedrock surface with a small cover fraction migrated downstream much

134   faster than those consisting of a higher fraction cover.

135   Despite these recent advances in modeling the morphodynamics of mixed bedrock-

136   alluvial rivers, there remain uncertainties about how differences in sediment and bedrock

137   roughness influence in mixed bedrock-alluvial rivers, and how hydraulics and macroroughness

138   features may interact to control alluvial patterns. Existing models are not able to resolve these

139   issues because either they are one-dimensional and unable to predict lateral variation in alluvial

140   cover, or they do not fully account for roughness effects of local sediment cover or transport. For

141   example, current models of mixed bedrock-alluvial morphodynamics have not been able to

142   predict persistent longitudinal alluvial strips, or to fully replicate the relationship between overall

143   sediment cover and the sediment supply to capacity ratio as reported in Chatanantavet and Parker

144   (2008).

145   This study intends to resolve the limitations models encounter when attempting to

146   simulate sediment dynamics in a mixed bedrock-alluvial channel by developing a new model

147   that uses: (1) a two-dimensional approach to account for the influence of potential bedforms

148   (e.g., alternate bars, antidunes, and dunes) in a straight channel; (2) the effect of flow resistance

149   partitioned into skin friction due to stationary particles and bedrock surface roughness, form drag

150   associated with dimensions of alluvial cover and irregular bedrock topography, and bedload

151   roughness produced by saltating sediment; (3) application of a ripple factor to take into account

152   for an intermediate state between the planar bed and small-scale bedforms.

153   We hypothesize that accounting for differential bedrock and sediment roughness,

154   roughness from sediment transport, form drag, and a near-bed shear stress correction are

155   necessary to capture sediment dynamics in mixed bedrock-alluvial channels. We use two

156   experiments to demonstrate that our model can reproduce observations made in fully alluvial and

157   mixed bedrock-alluvial channels, and we explore the importance of the different roughness terms

158   we include by repeating the simulation with those terms neglected. We simulate an experiment

159   of Lanzoni (2000) for alternate bar formation in an alluvial channel and an experiment of

160   Chatanantavet and Parker (2008) for gravel patch development in a mixed bedrock-alluvial

161   channel to assess model performance. Our model successfully replicates sediment dynamics in

162   both experiments. The numerical experiments that neglect form drag and transport components

163   of the roughness do not reproduce observations from the Chatanantavet and Parker (2008)

164   experiment, indicating that those components play a critical role in mixed bedrock-alluvial

165   sediment dynamics.

166   **2 Morphodynamic model**

167   We have developed a new morphodynamic model that simulates sediment transport and

168   deposition in mixed bedrock-alluvial channels. This model consists of three components: a

169   hydrodynamic model describing the depth-averaged flow field, a sediment transport model

170   describing bedload sediment transport rate, and a bed evolution model updating bed elevation

171   and the areal fraction of bedrock cover. Unlike previous models of mixed bedrock-alluvial

172   morphodynamics, this new model accounts for form drag and sediment transport roughness, in

173   addition to surface (grain and bedrock) roughness and a roughness-dependent critical Shields

174   stress. In addition, the total shear stress is corrected with a ripple factor in the sediment transport

175   model, as the bedform drag does not contribute to the bedload transport.

176   2.1 Flow model

177   The governing equations for calculating flow depth and velocity are composed of the

178   depth-averaged form of mass continuity and momentum balance in a 2D Cartesian coordinate

179   system:

180
$$\frac{\partial Q}{\partial t} + \frac{\partial F_x}{\partial x} + \frac{\partial F_y}{\partial y} = \frac{\partial D_x}{\partial x} + \frac{\partial D_y}{\partial y} + S_b + S_f \qquad (1)$$

181   where t is time, x and y are Cartesian coordinates, Q are the conservative variables, F_x and

182   F_y are the convective fluxes, D_x and D_y are the diffusive fluxes, S_b are the bed slope terms,

183   and S_f are the friction slope:

$$Q = \begin{bmatrix} h \\ hu \\ hv \end{bmatrix}, \quad F_x = \begin{bmatrix} hu \\ huu + \frac{1}{2}g\left(h^2 - z_b^2\right) \\ hvu \end{bmatrix}, \quad F_y = \begin{bmatrix} hv \\ huv \\ hvv + \frac{1}{2}g\left(h^2 - z_b^2\right) \end{bmatrix},$$

$$D_x = \begin{bmatrix} 0 \\ 2h(v+v_t) + \dfrac{\partial u}{\partial x} \\ h(v+v_t) + \left(\dfrac{\partial u}{\partial y} + \dfrac{\partial v}{\partial x}\right) \end{bmatrix}, \quad D_y = \begin{bmatrix} 0 \\ h(v+v_t) + \left(\dfrac{\partial u}{\partial y} + \dfrac{\partial v}{\partial x}\right) \\ 2h(v+v_t) + \dfrac{\partial v}{\partial y} \end{bmatrix},$$

$$S_b = \begin{bmatrix} 0 \\ -g\eta\dfrac{\partial z_b}{\partial x} \\ -g\eta\dfrac{\partial z_b}{\partial y} \end{bmatrix}, \quad S_f = \begin{bmatrix} 0 \\ -\dfrac{\tau_{bx}}{\rho} \\ -\dfrac{\tau_{by}}{\rho} \end{bmatrix}, \tag{2}$$

where h is the flow depth, u and v are the velocities in x- and y-directions, respectively, g is the gravitational acceleration, v and v_t are the kinematic viscosity of water and the turbulent eddy viscosity, respectively, η is the water surface elevation, z_b is the bed elevation, and ρ is the density of water. The bed shear stresses τ_{bx} and τ_{by} in x- and y-direction are given by

$$\left(\tau_{bx}, \tau_{by}\right) = \rho C_f \sqrt{u^2 + v^2}\,(u,v) \tag{3}$$

where C_f is a friction coefficient estimated using the law of the wall as a function of the flow depth h and total roughness height k_0:

$$C_f = \left[\frac{1}{\kappa}\ln\left(\frac{11h}{k_0}\right)\right]^{-2}. \tag{4}$$

193   2.2 Depth-averaged mixing-length model

194   The calculation of the turbulent viscosity term is based on a mixing-length model with

195   depth-averaged terms developed by Stansby (2003):

$$v_t = \sqrt{l_h^4 \left[2\left(\frac{\partial u}{\partial x}\right)^2 + 2\left(\frac{\partial v}{\partial y}\right)^2 + \left(\frac{\partial v}{\partial x} + \frac{\partial u}{\partial y}\right)^2 \right] + \left(\gamma u_* h\right)^2} \qquad (5)$$

197   where l_h is a horizontal mixing length scale ($l_h \approx 0.267\kappa h$), κ is the von Karman constant (

198    $\kappa \approx 0.408$), and γ is a constant that accounts for vertical mixing ($\gamma \approx 0.067$). The local shear

199   velocity, u_* , is defined as;

$$u_* = \sqrt{\tau_b / \rho} \qquad (6)$$

201   where $\tau_b = \sqrt{\tau_{bx}^2 + \tau_{by}^2}$ is the local bed shear stress vector, with components τ_{bx} and τ_{by} in the x -

202   and y -directions, respectively.

203   2.3 Bed roughness

204   The total roughness height k_0 is partitioned into three fractional roughness components,

205   including skin friction k_s , form drag k_f , and bedload transport k_t :

$$k_0 = k_s + k_f + k_t . \qquad (7)$$

207   The skin friction is induced by the viscous shear stress and pressure force acting on the

208   individual grains on the bed, and it relates to the size of the bed material. The local skin friction

209   roughness height varies with surface particle size in the completely alluvial channel and the

210   degree of irregularity of the bed surface in the bedrock channel. The calculation of skin friction

211   in the mixed bedrock-alluvial channel is based on the assumption that the skin friction is linearly

212   associated with the changes in the fraction of bedrock covered by alluvium:

$$k_s = P_c k_{sa} + (1 - P_c) k_{sb} \qquad (8)$$

214   where k_{sa} and k_{sb} are the hydraulic roughness height of the alluvial bed and bedrock bed,

215   respectively. The local areal fraction of alluvial cover $P_c = \eta_a / C_m \le 1$, in which $C_m = \pi d / 6$ is

216   the maximum volume of a monolayer of spherical sediment grains of constant diameter d

217   uniformly distributed over the bed surface (P. A. Nelson & Seminara, 2012), and η_a is the

218   thickness of the alluvial layer.

219   The form drag component of roughness results from the pressure force acting over entire

220   bedforms and is not responsible for the bedload motion of sediment particles (Maddux, McLean,

221   et al., 2003; Maddux, Nelson, et al., 2003). We calculate the form drag component of roughness

222   as a function of bed morphology through the empirical relation of Grant and Madsen (1982):

$$k_f = 30 a_r \frac{\eta_r^2}{\lambda_r} \qquad (9)$$

224   where η_r and λ_r are bed form height and wavelength, and a_r is a coefficient in the range from

225   0.3 to 3. Grant and Madsen (1982) suggested $a_r = 0.923$, which we use here.

226   For the sediment transport component of roughness, Wiberg and Rubin (1989) proposed

227   for the flat bed condition:

$$k_t = 30 \alpha_{ws} d \frac{a_1 T_*}{1 + a_2 T_*} \qquad (10)$$

229   where $T_* = \tau^*/\tau_c^*$ is the transport stage, τ^* is the dimensionless shear stress, τ_c^* is the critical

230   dimensionless Shields stress, $a_1 = 0.68$, $a_2 = 0.0204 \left(\ln 100d \right)^2 + 0.0220 \left(\ln 100d \right) + 0.0709$, and

231   $\alpha_{ws} = 0.056$. Here, the effect of local variation of bed topography is applied to the critical bed

232   shear stress to account for the gravity effect, as described in Section 2.5.

233   2.4 Bed deformation model

234   The local volumetric concentration of sediment per unit area is calculated using the

235   sediment conservation model for mixed bedrock-alluvial channel beds proposed by Luu,

236   Egashira, and Takebayashi (2004):

$$\frac{\partial V_{ba}}{\partial t} + \frac{\partial q_{bx}}{\partial x} + \frac{\partial q_{by}}{\partial y} = 0 \tag{11}$$

238   where V_{ba} is the total volume of sediment per unit area and q_{bx} and q_{by} are vectors of the

239   bedload transport rate per unit width in the x- and y-directions, respectively. The thickness of

240   the alluvial layer η_a and the volume of sediment in the bedload layer V_b are separately updated

241   considering the saturation volume of the bedload layer V_{bc}. This saturation volume is a threshold

242   value that determines whether the particles deposit on the bed or rapidly saltate over the surface

243   without resting on the bed. When V_{ba} exceeds V_{bc}, a volume of sediment equal to the difference

244   between V_{ba} and V_{bc} deposits on the bed as an alluvial layer. When V_{ba} is less than V_{bc}, the

245   particles pass over the bedrock surface as throughput load without deposition:

$$\eta_a = \begin{cases} \dfrac{V_{ba} - V_{bc}}{1 - \lambda} & \text{for} \quad V_{bc} \leq V_{ba} \\ 0 & \text{for} \quad 0 \leq V_{ba} < V_{bc} \end{cases} \tag{12}$$

247   where λ represents the porosity of the bed and V_{bc} is the saturation volume of the bedload layer

248   per unit area. When the bedrock is wholly exposed ($\eta_a = 0$), the volume of the throughput

249   bedload layer is lower than the saturation volume. When the bed is partially or fully covered with

250   sediment ($\eta_a > 0$), V_b equates to V_{bc} because sediment particles exchange occurs between

251   alluvial and bedload layers:

252
$$V_b = \begin{cases} V_{bc} & \text{for} \quad V_{bc} \leq V_{ba} \\ V_{ba} & \text{for} \quad 0 \leq V_{ba} < V_{bc} \end{cases}.$$
(13)

253   The saturation volume of bedload per unit area V_{bc} is defined by

254
$$V_{bc} = \frac{q_{bc}}{u_s},$$
(14)

255   where q_{bc} is the bedload transport capacity per unit width and u_s is the saltation velocity,

256   calculated here with the empirical excess shear stress relation presented in (Sklar & Dietrich,

257   2004):

258
$$\frac{u_s}{\sqrt{R_b g d}} = 1.56 \left(\frac{\mu \tau^*}{\tau_c^*} - 1 \right)^{0.56}$$
(15)

259   where $R_b = (\rho_s - \rho)/\rho$ denotes submerged specific gravity of sediment and ρ_s is the density of

260   the sediment. The bedload transport capacity per unit width q_{bc} is estimated using the relation

261   based on Ashida and Michiue (1972):

262
$$\frac{q_{bc}}{\sqrt{R_b g d^3}} = 17 \left(\sqrt{\mu \tau^*} - \sqrt{\tau_c^*} \right) \left(\mu \tau^* - \tau_c^* \right)$$
(16)

263   where dimensionless shear stress τ^* is defined as

264
$$\tau^* = \frac{\tau_b}{\rho R_b g d}$$
(17)

265   and $\mu \leq 1$ is the ripple factor, the ratio of the grain roughness to bed roughness (Ribberink, 1987)

266   (discussed further in Section 2.5).

267   The volumetric sediment transport rate per unit width in the x- and y-directions is

268   denoted

269
$$\left(q_{bx}, q_{by} \right) = q_b \left(\cos\alpha, \sin\alpha \right)$$
(18)

270   where α is the angle of bedload transport and the sediment transport intensity, q_b, depends on

271   the ratio of the volume of sediment and its saturation value. The bedload transport rate in

272   bedrock with a sufficient local volume of sediment equals the sediment transport capacity.

273   However, in bedrock rivers without sediment cover, the bedload transport rate is less than the

274   bedload transport capacity:

275
$$q_b = \begin{cases} \dfrac{V_b}{V_{bc}} q_{bc} & \text{for} \quad 0 \leq V_b < V_{bc} \\ q_{bc} & \text{for} \quad V_{bc} \leq V_b \end{cases}.$$
(19)

276   When considering the effect of gravity acting on particles for gradually varying bed

277   elevation, the sediment transport direction deviates from the direction of the boundary shear

278   stress. Here we adopt the well-known relationship (Struiksma, 1985):

279
$$\tan\alpha = \frac{\sin\delta - \dfrac{1}{\mathrm{f}\left(t^*\right)} \dfrac{\partial z_b}{\partial y}}{\cos\delta - \dfrac{1}{\mathrm{f}\left(t^*\right)} \dfrac{\partial z_b}{\partial x}}$$
(20)

280   where δ is the near-bed flow direction estimated to account for the influence of spiral water

281   motion induced by bed topography as

$$\delta = \tan^{-1}\left(\frac{v}{u}\right) - \tan^{-1}\left(A\frac{h}{r_s}\right), \tag{21}$$

283   where the local radius of depth-averaged stream curvature is

$$r_s = \frac{U^3}{u^2\dfrac{\partial v}{\partial x} + uv\left(\dfrac{\partial v}{\partial y} - \dfrac{\partial u}{\partial x}\right) - v^2\dfrac{\partial u}{\partial y}}, \tag{22}$$

285   where $U = \sqrt{u^2 + v^2}$ is the local flow velocity and the coefficient weighting the intensity of

286   helical flow is

$$A = \frac{2}{\kappa^2}\left(1 - \frac{\sqrt{C_f}}{\kappa}\right), \tag{23}$$

288   and $f(\tau^*)$ is a function weighting the influence of the bed slope, following the form proposed by

289   Talmon, Struiksma, and Van Mierlo et al. (1995):

$$f(\tau^*) = 9\left(\frac{d}{h}\right)^{0.3}\sqrt{\tau^*}. \tag{24}$$

291   2.5 Shear stress correction

292   The bedload sediment transport rate is expressed as a function of shear stress acting over

293   the channel bed. The presence of bedforms leads to a partial reduction of the total shear stress

294   related to the form drag, and the remainder is available for sediment transport. Traditionally this

295   has been implemented in models by multiplying the dimensionless shear stress by a so-called

296   "ripple factor." Several models for estimating the ripple factor have been proposed as a function

297   of the skin friction relative to the total friction (Ribberink, 1987; Vermeer, 1986):

298

$$\mu = \left(\frac{C_{fs}}{C_f}\right)^{n/2} \tag{25}$$

299   where C_{fs} is the friction coefficient accounting for skin friction obtained by substituting k_0 with

300     $k_s + k_t$ in equation (4), and the exponent n is defined by

301

$$n = 1.8 + 0.27 \log q^*, \tag{26}$$

302   where $q^* = q_{bc}/\sqrt{R_b g d^3}$ is the dimensionless bedload transport rate. This relationship is valid for

303     $0.001 \le q^* \le 1$ (Vermeer, 1986).

304   2.6 Critical dimensionless Shields stress

305   Flume experiments conducted in bedrock channels (Inoue et al., 2014; Mishra & Inoue,

306   2020) have related the channel roughness and dimensionless critical shear stress of sediment

307   movement. A power approximation proposed by Mishra and Inoue (2020) is applied to this

308   model to take into account the effect of total hydraulic roughness on critical shear stress:

309

$$\tau_{c0}^* = \tau_{c\alpha}^* \left(k_s/d\right)^{0.6} \tag{27}$$

310   where $t_{c\alpha}^*$ is the critical Shields stress back-calculated from sediment transport capacity

311   measured from the experiment in the flat channel. In addition to the bed roughness, the local bed

312   slope effect on the initiation of particle motion can be added because the local bed slope provides

313   a gravitational component of the force exerted on the particle (Duan & Julien, 2005; Soulsby,

314   1997):

315
$$\frac{\tau_c^*}{\tau_{c0}^*} = \frac{\sin\left(\phi + \beta_s\right)}{\sin\phi} \frac{\cos\beta_n}{\sqrt{1 - \tan^2\beta_n / \tan^2\phi}} \tag{28}$$

316 where ϕ is the grain angle of repose and β_s and β_n are the slope in the streamwise and cross-

317 stream direction of the sediment transport, respectively. A simple approach was proposed by

318 Wiberg and Smith (1987) for the treatment of heterogeneous bed conditions through the

319 geometric relation of friction angle as a function of particle size to the roughness length scale of

320 the bed:

321
$$\phi = \cos^{-1}\left(\frac{d/k_s - 0.02}{d/k_s + 1}\right) \tag{29}$$

322 The bed slopes in the streamwise and cross-stream direction of sediment transport are

323
$$\beta_s = \tan^{-1}\left(\frac{\partial z}{\partial x}\cos\alpha + \frac{\partial z}{\partial y}\sin\alpha\right), \quad \beta_n = \tan^{-1}\left(\frac{\partial z}{\partial y}\cos\alpha - \frac{\partial z}{\partial x}\sin\alpha\right). \tag{30}$$

324   2.7 Solution procedure

325   The model uses a decoupled approximation of the morphodynamic system by assuming

326 that the response time of the bed evolution is relatively long compared to the time scale of the

327 hydraulic processes (De Vries, 1965; Defina, 2003; J. M. Nelson & Smith, 1989). Therefore the

328 hydrodynamic solver is followed by the calculation of the modified Exner equation.

329   First, local water depth and flow velocity are calculated using the hydrodynamic model

330 (equation (1) - (2)). The friction term is estimated by taking into account the roughness of the

331 bedrock k_{sb} and alluvial surfaces k_{sa}, topographic variability k_f, and the effect of saltating

332 grains during sediment transport k_t. Flow-conservative variables (h, hu, and hv) at each cell

333   interface are calculated using the total variation diminishing (TVD) scheme (Toro, 2009) for

334   cell-centered advection terms (F_x and F_y).

335   Second, the local sediment transport rate q_b (equation (19)) is estimated considering the

336   local circumstance of sediment deposition, which is determined by the fraction of bedrock cover

337   P_c (equation (14) - (16)). The depth-averaged flow variables (h, u, v, and k_s) determine the

338   threshold of incipient sediment motion (τ^* and τ_c^*), then the local bedload transport rate q_b,

339   grain saltation velocity u_s, and saturation volume of the bedload layer V_{bc} are calculated.

340   Third, the sediment flux divergence updates the total sediment volume per unit area

341   (equation (11)). Finally, the new alluvial layer thickness η_a and the volume of bedload transport

342   per unit area V_b are determined by whether the bedrock is covered by alluvium or exposed

343   (equation (12) - (13)).

344   **3 Model validation**

345   We set up two simulations to demonstrate the model's ability to replicate observations in

346   both alluvial and mixed bedrock-alluvial conditions. These benchmark laboratory flume

347   experiments documented: (1) the development of alternate bars in fully alluvial channels

348   (Lanzoni, 2000); and (2) flow and sediment transport in mixed bedrock-alluvial channels

349   (Chatanantavet & Parker, 2008). Table 1 summarizes the conditions for each experiment.

350   3.1 Alternate bar formation in an alluvial channel

351   To demonstrate alternate bars in alluvial conditions, we simulate Run P1505 described in

352   Lanzoni (2000). In the experiment, a straight, flow- and sediment-recirculating flume 1.5 m

353   wide, 1 m deep with a 55 m long test section was supplied with a steady water discharge of 30

354   l/s. The bed was composed of a uniform sand size of 0.48 mm and initially screeded flat. At the

355   upstream end of the channel, a 16 m long, 5 m wide stilling basin was installed to ensure smooth

356   and regular water and sediment discharge into the experimental channel. This experiment

357   stopped as it reached equilibrium after 28 hours, when the water surface slope matched the bed

358   slope. A summary of reach-averaged measurements is reported in Table 1. Alternate bars were

359   formed with an average height of 7 cm, wavelength of 10 m, and celerity of 2.80 m/h.

360   Our simulation of Run P1505 is conducted with some modification of experimental

361   conditions. First, a longer channel of 120 m was used to ensure the bar reached the equilibrium

362   state before migrating out of the domain (Defina, 2003). Second, a small topographic bump 0.6

363   m long, 0.75 m wide, and 5 mm high was introduced near the upper boundary on the left side

364   (looking downstream) to create an initial disturbance to induce free bar development because the

365   arbitrarily distributed source of disturbances from the physical experiment was unknown.

366   Numerical models generally require perturbations such as a topographic bump (Defina, 2003;

367   Wu et al., 2011) or a bend upstream of the straight channel (Mendoza et al., 2017) to develop

Table 1. Summary of Experimental Conditions.[a]

	m	m	%	l/s	g/s	mm	cm	m/s	hr
Run	B	L	S	Q_w	Q_c	D	H	U	t
P1505[b]	1.5	55	0.452	30	28	0.48	4.4	0.45	28
2-B2[c]	0.9	13	2	55	110	7	5.5	1.02	5

[a] B is the channel width, L is the channel length, S is the channel slope, Q_w is the water discharge, Q_c is the sediment transport capacity, D is the grain size, H is the averaged flow depth, U is the averaged flow velocity, and t is the duration of the experiment.
[b] Run P1505 was performed by Lanzoni (2000).
[c] Run 2-B2 ($q_s/q_c = 0.56$) was performed by Chatanantavet & Parker (2008).

368   bars in uniform flow over flat-bed conditions. Third, the constant and uniform water discharge

369   and sediment feed rate were imposed at the inlet.

370   3.2 Patterns of bedrock alluviation with limited sediment supply

371   The second experiment Run 2-B2 ($q_s/q_c = 0.56$) (Chatanantavet & Parker, 2008), was

372   carried out on a non-erodible bedrock surface in a 13 m long and 0.9 m wide straight, rectangular

373   flume channel with a slope of 0.02. The bedrock bed was randomly abraded with a longitudinally

374   averaged standard deviation of 2.4 mm, and the distance between the lowest and highest points

375   of the profile is approximately 1 cm (Figure 1b and 3b in Chatanantavet & Parker, 2008).

376   The averaged values of initial experimental conditions are presented in Table 1. The

377   representative hydraulic roughness of the bedrock surface was back-calculated from the

378   Manning-Strickler relation under the flow conditions measured from the experimental results

379   conducted in the channel slope of 0.0115. Initially, the bed was covered entirely with a 2 cm

380   thick layer of uniform 7 mm sediment. The steady water discharge was 55 l/s, the constant

381   sediment supply rate was 62 g/s, and the sediment transport capacity was estimated at 110 g/s for

382   a wholly covered bed. The experiment stopped when the fraction of bedrock cover P_c reached a

383   steady state whose value was approximately 0.59.

384   The numerical model simulation of this experiment uses a 0.9 m wide, 20 m long bedrock

385   bed with randomly generated topographic perturbations with a standard deviation of 2.2 mm and

386   a peak-to-peak distance of bed elevation of 0.9 cm (Figure 1). The roughness height due to skin

387   friction (grain equivalent roughness height) used in the numerical simulation was back calculated

388   from equation (4) using experimentally measured average flow conditions for each case of bare

389   bedrock bed k_{sb} and alluvial bed k_{sa}. In the channel fully covered with sediment $H = 0.06$ m

390   and $U = 1.02$ m/s, and in case of flow over bare bedrock bed $H = 0.05$ m and $U = 1.22$ m/s,

391   hence k_{sa} =7 mm and $k_{sb} = 3$ mm. The sediment supply to transport capacity ratio q_s/q_c is 0.6,

392   which means the steady sediment supply rate is 66 g/s assuming the sediment transport capacity

393   of the alluvial bed is 110 g/s. A small perturbation was given by changing sediment distribution

394   patterns at the upstream end of the channel to prevent sediment and bedform from washing out

395   from the upstream end of the channel (e.g., Figure 14 in Inoue et al., 2016).

396   3.3 Simulations investigating impacts of roughness components on mixed bedrock-

397   alluvial sediment dynamics

398   To investigate the importance of different roughness components on the model's

399   performance of predicting alluvial patterns, we conducted numerical simulations without

400   bedform roughness or ripple factor under the same conditions of Run 2-B2. The form drag effect

401   on the flow is removed by setting the bedform roughness to zero; hence the ripple factor is no

402   longer influential. The effect of bed-form solely on sediment transport is removed by setting the

403   ripple factor to unity.

404   We also conducted a simulation where the sediment transport roughness was set to zero,

405   to explore how that component influences morphodynamic predictions in mixed bedrock-alluvial

406   channels. For this simulation, the total roughness consisted of bedform and grain roughness, the

407   latter of which was increased relative to the base scenario so that overall flow depths and
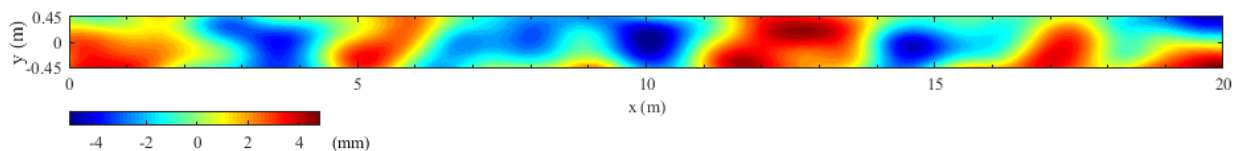
408   velocities still matched experimental observations.

Figure 1. Plan view of bedrock topography. Colorbar scale indicates the detrended bed elevation.

409   **4 Results**

410   4.1 Simulation of alluvial alternate bars (Run P1505)

411   Figure 2 shows the plan views of the evolution of detrended bed surface elevation in Run

412   P1505. The initial upstream bump ($t = 0$ h) deflects flow and sediment transport. The sediment

413   eroded from the bump forms the first bar and triggers the development of smaller bars

414   downstream ($t = 2$ - 4 h). The bars get larger and taller as they migrate downstream. When they

415   reach equilibrium, their downstream migration and growth rate vary slowly and become stable.

416   The initially flat alluvial bed, during the bedform formation and migration process, develops into

417   a clear pattern of alternate bars. The initial disturbance gradually spreads out by decreasing

418   height and stretching in the flow direction, prompting new bars to develop downstream (e.g.,

419   Figure 3 in Defina, 2003).

420   The longitudinal bed profiles and the bed elevation difference between the right- and left-

421   side walls from the numerical results (Figure 3) can be compared to the measured data at the

422   equilibrium state from Lanzoni (2000, Figure 1g) (Figure 4). Bar amplitudes are calculated as the

423   difference between the right and left side of the bed elevation, measured 20 cm from each side

424   wall (Figure 3a, b). The amplitude and wavelength are calculated using half the vertical and

425   twice the horizontal peak-to-peak distances of the detrended profile. The celerity of migrating
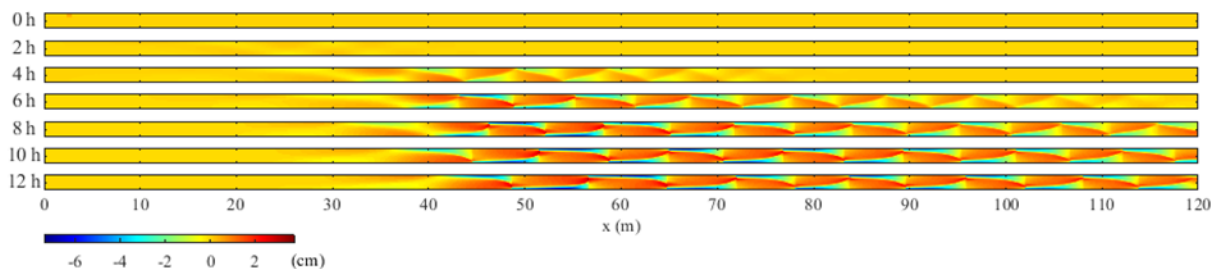

Figure 2. Detrended plan view of modeled bed evolution for the alluvial bar flume experiment (P1505) with the same longitudinal and transverse scale. Colorbar shows detrended bed elevation at the same scale for all plots.

426   bars is calculated by tracking topographic peaks over time. The longitudinal bed profiles from

427   numerical experiments exhibit highly ordered wave patterns. The axis bed profiles in the

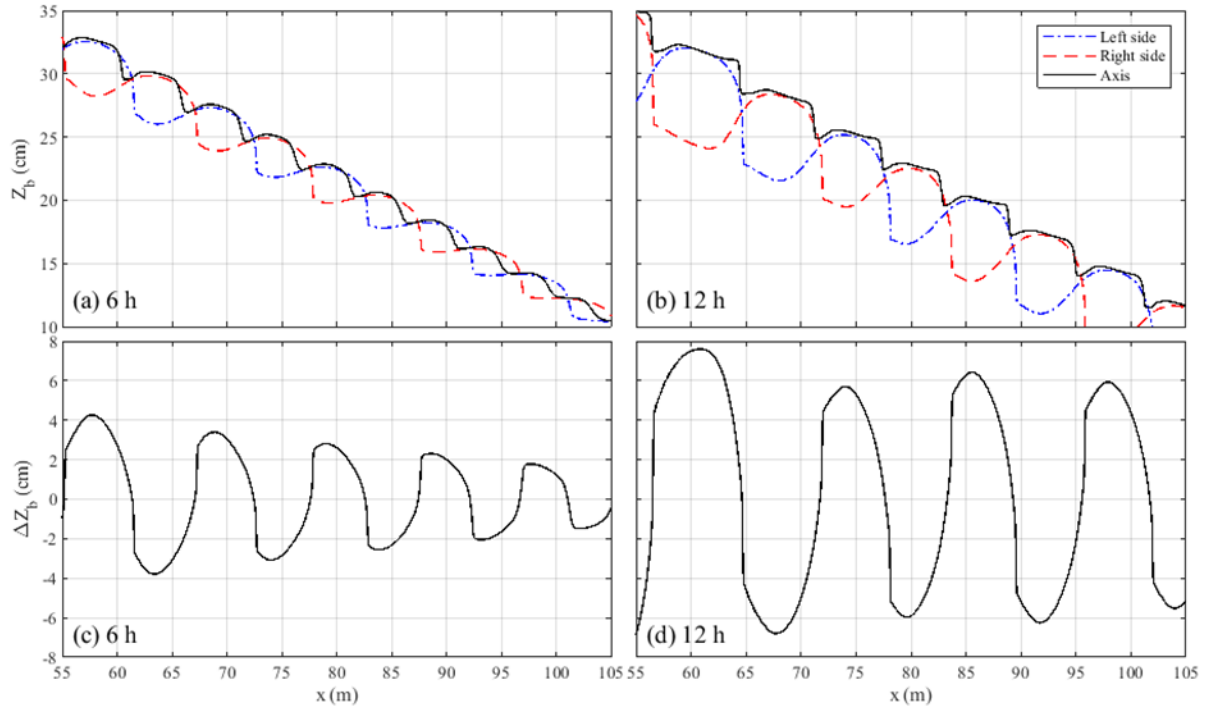428   numerical simulation and experiment indicate the transversally maximum value of bed elevation.

Figure 3. Modeled longitudinal bed profiles along the left- and right-side wall and axis at 6 h (a) and 12 h (b) and the difference between right- and left-side bed elevation at 6 h (c) and 12h (d).
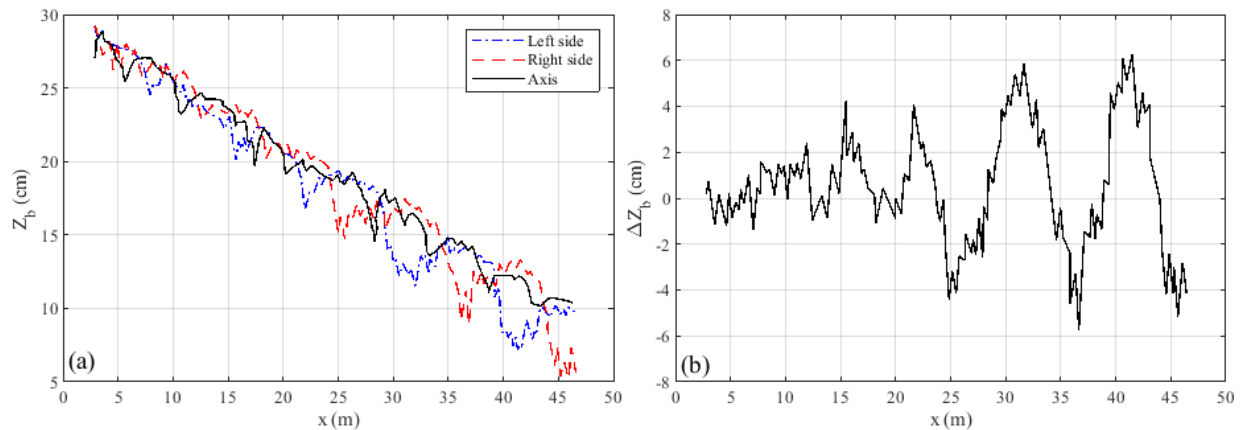

Figure 4. Measured (a) longitudinal bed profiles along the left- and right-side wall and (b) the difference between right- and left-side bed elevation at equilibrium (Figure 1g, Lanzoni, 2000).
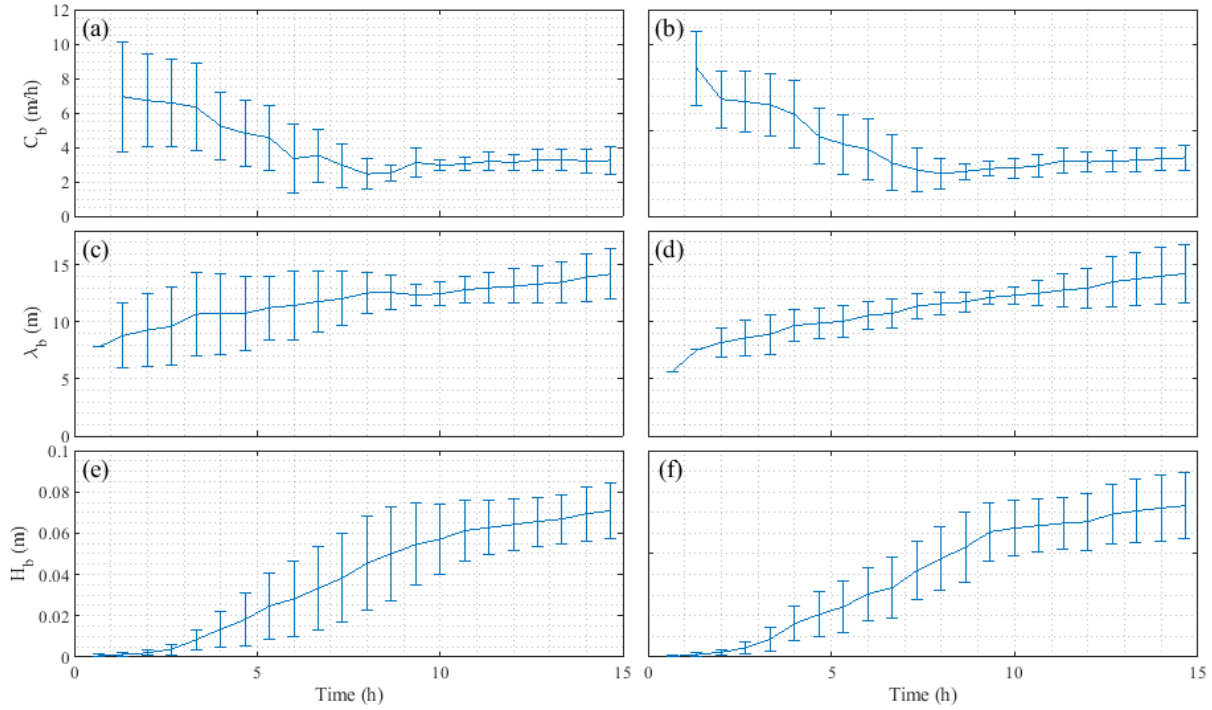
Figure 5. Computed time evolution of bar characteristics; celerity, wavelength, and amplitude (from top to bottom) on the left (a, c, and e) and right (b, d, and f) side of the channel.

Table 2. Comparison of Bar Characteristics from Measured Data and Computed Results.

	m/h	m	cm
Run	C_b	λ_b	H_b
P1505	2.8	10	7
Computed	3.2$\pm$0.5	14$\pm$2	7$\pm$1

429   As the calculated time changes in bar celerity (Figure 5a, b), wavelength (Figure 5c, d),

430   and amplitude (Figure 5e, f) are small, and we consider the bed condition at near equilibrium.

431   The mean characteristics of the bar (bar height, wavelength, and celerity) near equilibrium are

432   compared and reported in Table 2. The computed bar wavelength, height, and celerity are

433   approximately 14 m, 7 cm, and 3.2 m/s, respectively. The computed bar height and celerity show

434   reasonably good agreement with observations of Lanzoni (2000), but the wavelength is slightly

435   overestimated. However, the computed alternate bar wavelength is approximately nine times the

436   channel width showing good agreement with Defina's (2003) numerical result and laboratory

437   data of alternate bar wavelength prediction (Ikeda, 1984).

438   4.2 Simulation of mixed bedrock-alluvial experiment (Run 2-B2)

439   Figure 6 shows a series of numerical results illustrating the time evolution of bed

440   configuration for the mixed bedrock-alluvial experiment (Run 2-B2) commencing from a 2 cm

441   thick alluvial cover ($t = 0$ h). The non-uniform sediment distribution, feeding more sediment at
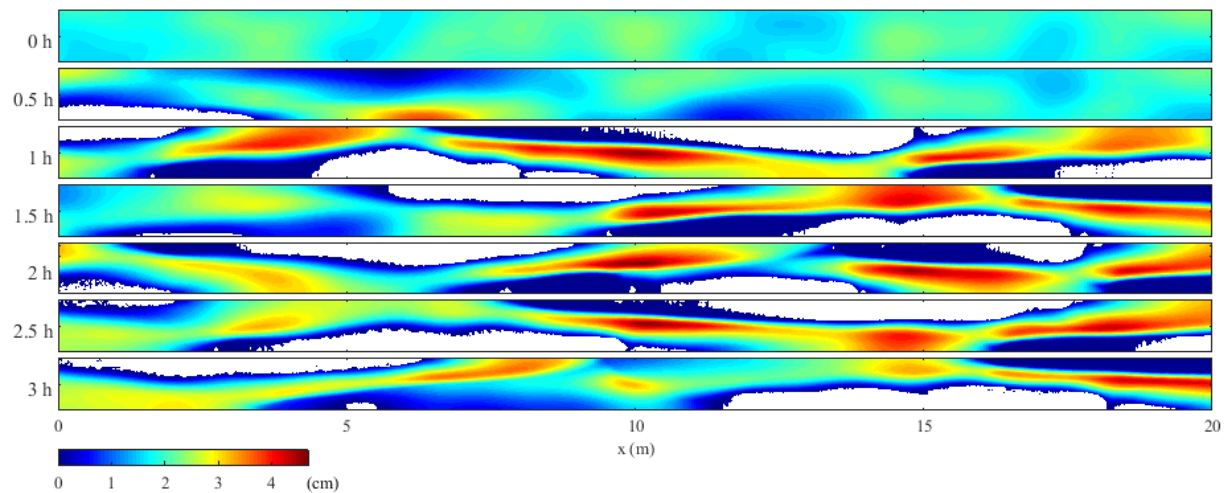

Figure 6. Simulated bed evolution of Run 2-B2. Colorbar shows the thickness of the sediment cover, and white areas correspond to the exposed bedrock surface.
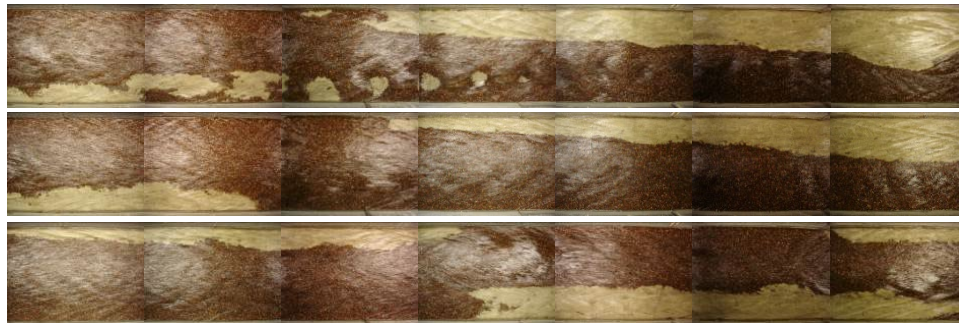

Figure 7. Time evolution of bedrock exposure Run 2-B4 at times are 1 ,4, and 7 hourse from top to bottom: Q_s= 97 g/s, q_s/q_c= 0.88, and P_c = 0.78 (Chatanantavet & Parker, 2008 (personal communication)). The channel is 0.9 m wide, 13 m long, water and sediment flow from left to right, and light and dark areas correspond to bedrock and sediment, respectively.

442   one side than the other, causes flow deflection induced by a laterally sloping bed at the upstream

443   end ($t = 0.5$ h). At an early stage, this disturbance quickly erodes sediment on the right side of the

444   channel down to the bedrock bed and creates pools and bars downstream. Then the exposed

445   bedrock bed area, indicated as a white area, increases as the pools deepen and bars grow taller (t

446    $= 1$ h). The sediment on the bed forms a strip of sediment shifting from one side to the other side

447   of the channel through time while maintaining a consistent fraction of bedrock cover. Similar

448   patterns were observed in the Chatanantavet and Parker (2008) experiments; for example, Figure

449   7 shows the time evolution of bedrock exposure from Run 2-B4 (Table 1 in Chatanantavet and

450   Parker, 2008) with $Q_s = 97$ g/s, $q_s/q_c = 0.88$, and $P_c = 0.78$ at equilibrium phase. Again, a

451   continuous band of sediment forms comparable to Figure 6. However, the sediment cover is

452   more expansive, and the bed sediment shifting from one to the other side is less sensitive because

453   of the higher sediment supply rate than what was provided in Run 2-B2 modeled here.

454   Figure 8 shows the computed flow variables, bed topography, and sediment transport

455   capacity at equilibrium ($t = 5$h). The flow depth and velocity over the exposed bedrock area are

456   higher than on the alluvial bed. However, calculated shear stress is lower in exposed bedrock

457   areas due to the smaller roughness and higher flow depth. The critical dimensionless shear stress

458   is generally higher on the alluvial bed but smaller over the lee side of the bedforms. The

459   sediment transport capacity tends to be higher over the exposed bedrock surface and stoss side of

460   the bedform and lower on lee slopes.

461   Figure 9 shows the time evolution of channel averaged fraction of bedrock exposure

462    $F_e = 1 - P_c$, alluvial thickness, relative Shields parameter, and bedload transport rate. A ratio of

463   alluvial coverage of bed surface in the area of interest determines the fraction of bedrock covered

464   with sediment $P_c = A_c/A_t$ (Johnson, 2014), where A_c is the area covered with sediment and A_t

465   is the total area of interest, or numerically $P_c = \sum P_{ci}/N$, where P_{ci} is the local fraction of

466   bedrock cover (equation 8) and N is the total number of cells in the domain. The fraction of

467   bedrock exposure is initially zero when the bed is entirely covered by sediment and quickly

468   converges toward a near-equilibrium state where F_e is 0.4 at $t = 1$ h (Figure 9a). The numerical

469   result of the degree of bedrock exposure presents a similar value of F_e to the experimental

470   observation. The averaged sediment cover thickness over an alluvial area varies little in the range
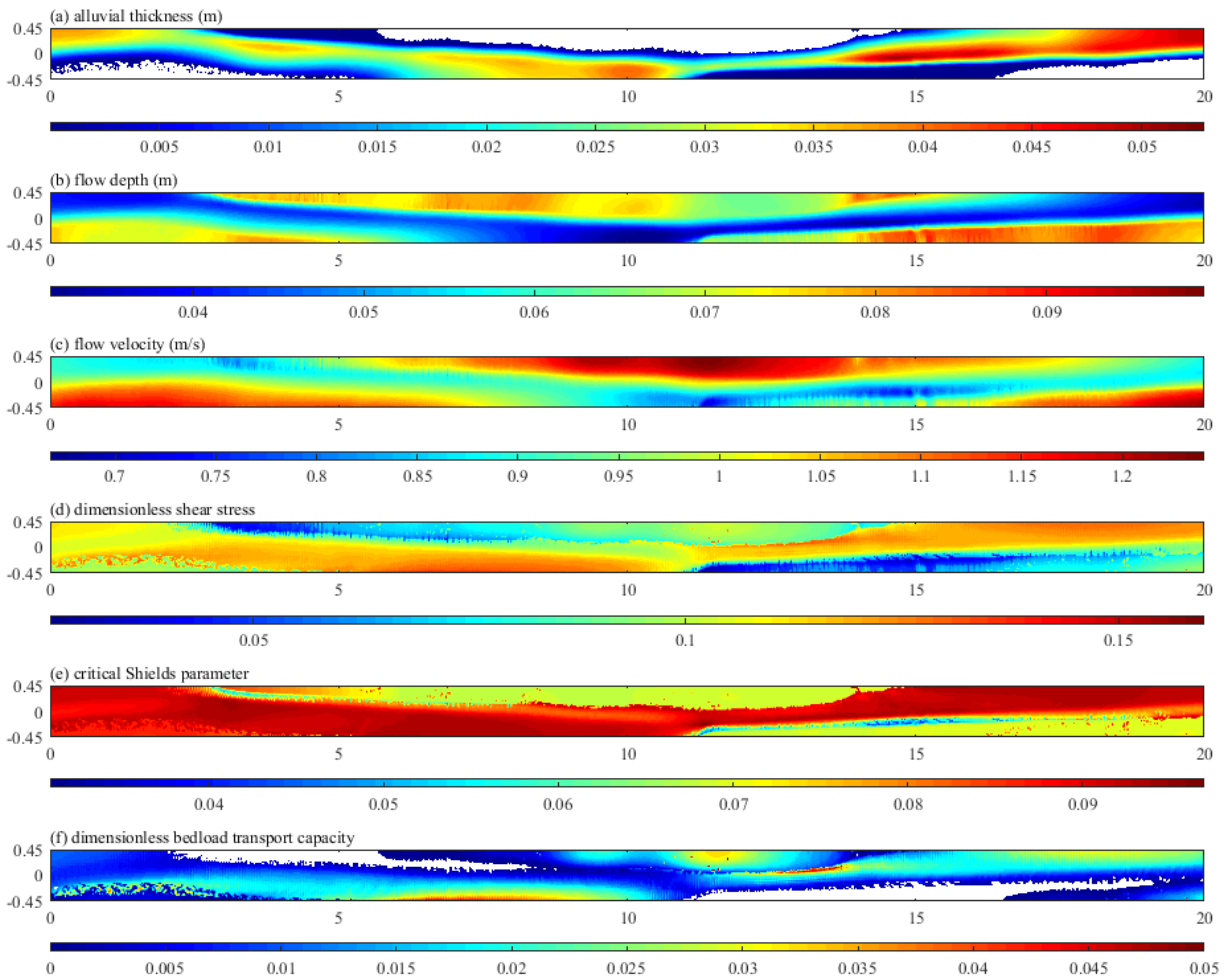

Figure 8. Plan view of (a) alluvial thickness, (b) flow depth. (c) flow velocity, (d) dimensionless shear stress, (e) critical Shields parameter, and (f) dimensionless bedload transport capacity at $t = 5$ h. Colorbars indicate the scale of computed values, respectively, and white areas correspond to (a) the exposed bedrock surface and (e) zero sediment transport rate.
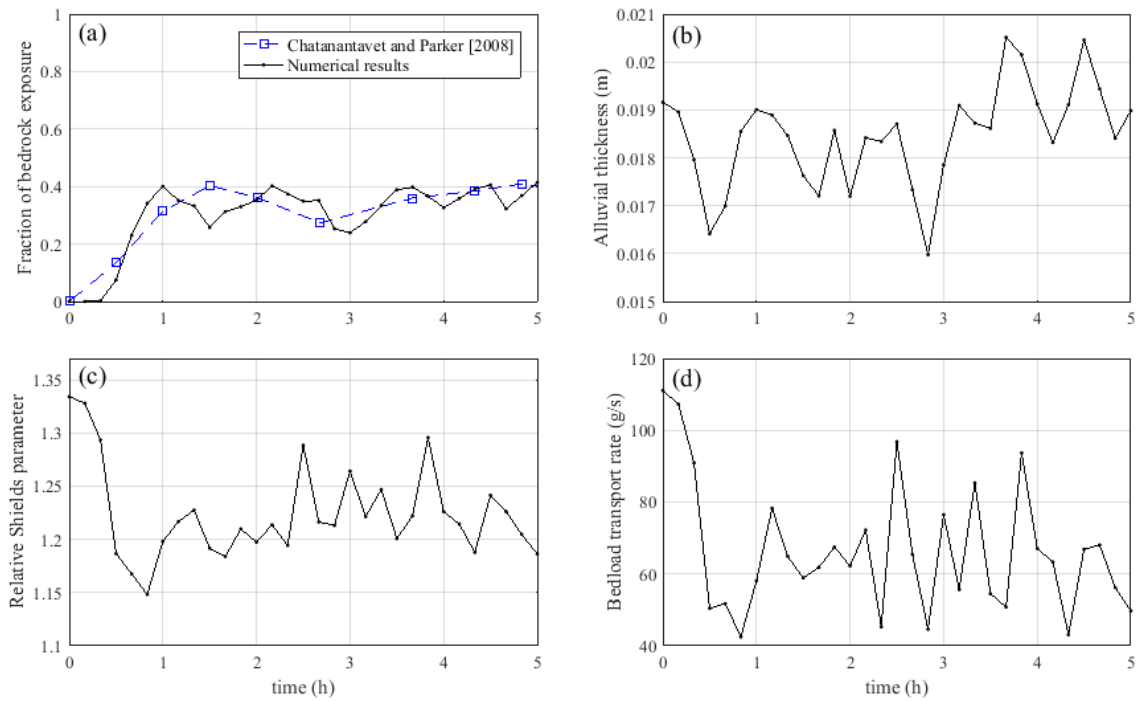
Figure 9. The time evolution of the (a) fraction of bedrock exposure from numerical and experimental results, (b) averaged alluvial thickness over the part of the bed covered with sediment, (c) relative Shields parameter, and(d) sediment transport rate.

471   of a single grain diameter (Figure 9b). The relative Shields parameter τ^*/τ_c^* (Figure 9c) and

472   bedload transport rate (Figure 9d) decrease from an initially higher value to approximate

473   equilibrium and vary around 1.2 and 70 g/s, respectively.

474   The comparison between the computed and measured quantities available from

475   experimental observations is presented in Table 3. The agreement is reasonably good in

476   predicting the fraction of bedrock cover, but higher flow depth and lower velocity in the

477   experiment result in a lower Froude number and lower dimensionless shear stress. The model

478   predicted lower shear stress over the bare bedrock areas than the alluvial areas because the

479   bedform developed during the simulation. The alluvial bars form where flow depth is low and

480   velocity is high, and pools exist over the bare bedrock area with deep flow depth and low

481   velocity.

Table 3. Summary of Numerical Results

Run	P_c	cm	m/s		
		H	U	Fr	τ^*
2-B2 (C&P)[a]	0.59	5.5±1.5	1.11	1.51	0.11
2-B2[b]	0.60	6.0	1.00	1.32	0.10
2-B2 (covered zones)[c]		5.6	0.95	1.31	0.10
2-B2 (exposed zones)[d]		7.5	1.07	1.26	0.08

[a] Experimental results from Chatanantavet and Parker (2008).
[b] Reach averaged numerical results.
[c] Reach averaged numerical results only over the alluviated zones.
[d] Reach averaged numerical results only over the exposed bedrock zones.

5 Discussion

The present study shows the results that bed topography comparable to experimental

observations from (1) free bar formation in a mild slope alluvial channel with fine grains

(Lanzoni, 2000) and; (2) alluvial pattern in the mixed bedrock-alluvial channel in a steep slope

channel with coarse grains (Chatanantavet & Parker, 2008). These suggest that the model can

simulate complex flow and sediment transport to gain insight into mechanisms of the bedform

development and alluviation patterns in mixed bedrock-alluvial channels.

The discrepancies between the numerical and experimental results are mainly associated

with the initial and boundary conditions, which are not successfully reflected in the numerical

models, such as the size of the initial disturbances and patterns of flow and sediment distribution

at the channel inlet.

493   5.1 Discussion on ripple factor and form drag

494   Only a few studies have attempted to simulate sediment transport in a straight mixed

495   bedrock-alluvial channel using a 2D numerical model (Inoue et al., 2016; P. A. Nelson &

496   Seminara, 2012). These models estimated bed resistance to the flow using the grain roughness

497   and bedrock surface irregularity which is applicable to the plane bed. Our model includes the

498   effect of bed-form generation in roughness estimation since alternate bars often form in mixed

499   bedrock-alluvial channels (Chatanantavet & Parker, 2008; Inoue et al., 2016; P. A. Nelson &

500   Seminara, 2012). The hydraulic roughness height of alluvial bed changes according to the size of

501   bedforms (i.e., dunes and ripples) (Engelund, 1977; Raudkivi, 1997; van Rijn, 1982, 1984;

502   Vanoni & Hwang, 1967; Wiberg & Nelson, 1992).

503   Figure 10 shows the time evolution of bed topography with the same condition applied in

504   Run 2-B2 without including the bedform effect in the roughness calculation, and hence the

505   ineffective ripple factor. This simulation undergoes sediment washing out from the upstream end

506   of the channel while forming a bar-like bedform downstream. This result is comparable with the

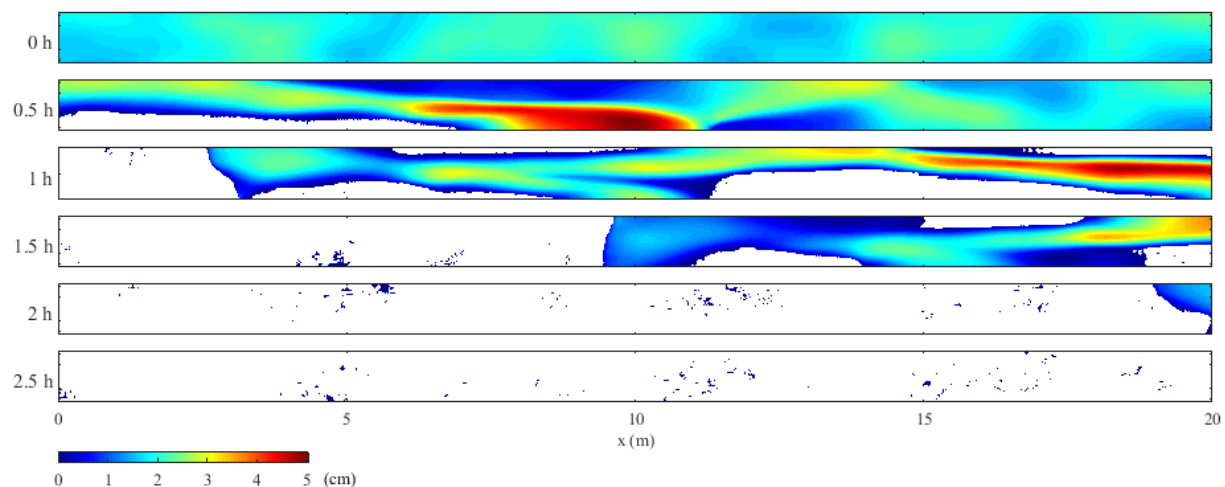507   results provided by Inoue et al. (2016).

Figure 10. The time evolution of bed exposure for run 2-B2 without form drag effect ($k_f = 0$). Colorbar means alluvial cover thickness, and white area is exposed bedrock surface.

508   The prediction of bedload transport is based on the corrected dimensionless shear stress

509   for bedform roughness with a ripple factor (Meyer-Peter & Muller, 1948). The value of the

510   ripple factor has not been reported explicitly but empirically estimated as a ratio of grain shear

511   stress to the total bed shear stress (Ribberink, 1987; Vermeer, 1986). Nevertheless, the ripple

512   factor is often applied to sediment transport models to generate bedforms in alluvial channels

513   with a constant value of less than 1 (Defina, 2003; Van der Meer et al., 2011).

514   Figure 11 shows the plan view of the bed topography of Run 2-B2 without the

515   dimensionless shear stress correction by using a ripple factor equal to 1 in equation (16). The

516   upstream sediment erodes slower than the bed evolution in Figure 10, and the morphodynamic

517   process has enough time to form a longitudinal sediment strip because the form drag generates

518   higher flow resistance. However, larger dimensionless shear stress due to the absence of the

519   ripple factor in the supply-limited channel causes a thin layer of sediment at the upstream end

520   and a narrow strip of sediment. The strip of sediment is cut off at the narrowed section, and the
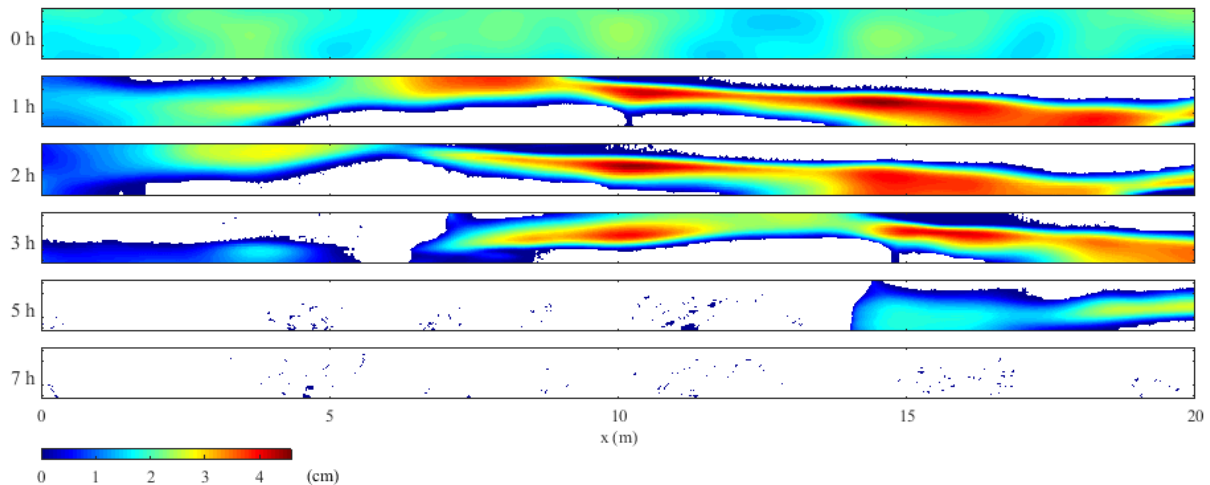
521   sediment is eventually washed out.

Figure 11. The time evolution of bed exposure for Run 2-B2 without ripple factor ($\mu = 1$).
Colorbar indicates alluvial cover thickness, and the white area is exposed to the bedrock surface.

522   Comparing Figures 6 and 10-11, it can be seen that introducing both form drag to the

523 roughness and ripple factor of the shear stress in bedload transport is critical in developing

524 bedforms and persistent alluviation in bedrock channels where the sediment supply is less than

525 the capacity of the channel. Results from previous models attempting to replicate these

526 experiments (Inoue et al., 2014) show alternate bar development over the alluvial surface, but

527 sediment supply less than the transport capacity decreases the thickness of the alluvial layer

528 leading to sediment washing out from upstream and exposure of the entire bedrock.

529   The roughness component for form drag effectively increases drag and reduces flow

530 velocity, whereas the ripple factor reduces shear stress in bedform-developed areas. Unlike the

531 form drag acting on entire bedform fields, skin friction is responsible for the local bed surface

532 roughness only. The smaller surface roughness over the exposed bedrock area than over the

533 alluvial area produces higher shear stress. Therefore the model absent of form drag and ripple

534 factor predicts a higher sediment transport rate as the fraction of sediment cover decreases in

535 limited sediment supply conditions, resulting in a total washout of the sediment from the

536 channel.

537   5.2 The impact of sediment transport roughness

538   Our model explicitly accounts for both the grain roughness and roughness produced by

539 moving particles (Dietrich, 1982; Grant & Madsen, 1982; Smith & McLean, 1977; Wiberg &

540 Rubin, 1989). To explore the importance of accounting for each of these components

541 individually, we conducted a simulation where we ignored sediment transport roughness and

542 increased the grain roughness to compensate for reduced bed roughness caused by the absence of

543 sediment transport roughness.

544   Figure 12 shows the time evolution of bed topography for this simulation of Run 2-B2,

545   excluding sediment transport roughness. A strip of sediment forms shifting from one side to the

546   other side of the channel momentarily ($t = 0.5$ h), but then washes out from the upstream end of

547   the channel ($t = 2$ h), with a small residual alluvial patch persisting only in a topographic low

548   area in the bedrock ($t = 4$ h). The flow resistance decreases as bedrock gets exposed because of

549   the underlying linear relationship between the fraction of bedrock cover and grain roughness.

550   Unlike grain roughness, the sediment transport roughness is larger where grain movements

551   actively take place. The sediment transport roughness tends to be higher over the bedrock surface

552   partially covered with sediment because the sediment transport rate over the smoother bedrock

553   surface, where the flow velocity is faster, is higher than over the rougher alluvial surface. The

554   sediment transport roughness contributes to the formation of alluvial patches in the bedrock

555   channel by reducing grain entrainment over the mixed bedrock-alluvial surface. These results

556   indicate that separate accounting of grain and sediment transport roughness produces

557   morphodynamic predictions that better match observations of persistent alluvial patterns in
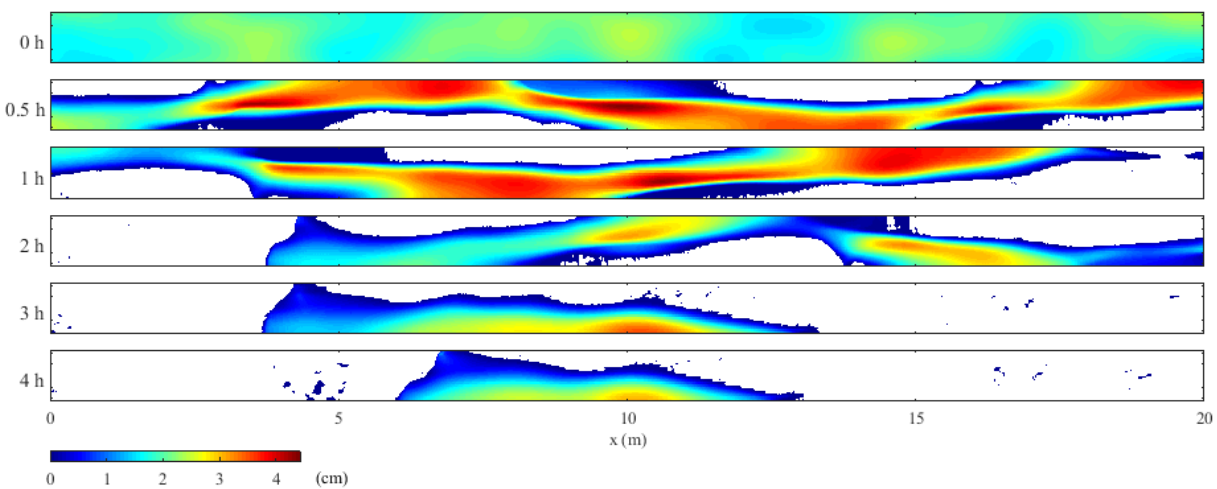
558   mixed bedrock-alluvial channels.

Figure 12. The time evolution of bed exposure for Run 2-B2 without sediment transport roughness from flow resistance $(k_t = 0)$. Colorbar indicates alluvial cover thickness, and the white area is exposed to the bedrock surface.

559 **6 Conclusions**

560   In this study, we have developed a two-dimensional morphodynamic model to explore

561 bar formation and migration in an alluvial channel and sediment transport mechanisms in a

562 mixed bedrock-alluvial channel without sufficient sediment supply. Comparisons of model

563 predictions with experimental observations from the free bar test show that the model predicts

564 bed morphology and bedform development similar to the observations of the flume experiment.

565 However, some discrepancies raise the need for proper tuning of model parameters and initial

566 bottom perturbation.

567   The model predicts the flow field and sediment distribution patterns in mixed bedrock

568 alluvial channels reasonably well. Numerical experiments show that the inclusion of bedform

569 roughness and a shear stress correction for near-bed sediment transport is critical to be able to

570 replicate the alluvial patterns over bare bedrock observed in flume experiments. The evolving

571 interactions between the alluvial and bedrock bed surface, flow field, and sediment transport

572 simultaneously modify the degree of sediment cover and bed topography. The numerical model

573 presented in this study captures the behavior associated with the bedrock alluviation process and

574 can be used to extend its applicability to various flow and sediment supply conditions with

575 different channel slopes and antecedent topography.

576   Future work could explore the mechanisms of sediment pattern formation in mixed

577 bedrock-alluvial rivers and characterize the effects of the channel slope, initial sediment cover

578 thickness, difference between the grain and bedrock roughness, and bedrock configuration.

579 **Acknowledgments**

582   **Open Research**

583   The code demonstrating the 2D morphodynamic model and numerical data of test cases shown

584   herein are archived at https://github.com/rcemorpho/morph2d.

585   **References**

586   Ashida, K., & Michiue, M. (1972). Hydraulic Resistance of Flow in an Alluvia Bed and Bed

587   Load Transport Rate. *Proceedings of Japan Society of Civil Engineers*, 59–69.

588   https://scirp.org/reference/referencespapers.aspx?referenceid=1312271

589   Bernini, A., Caleffi, V., & Valiani, A. (2006). Numerical Modelling of Alternate Bars in Shallow

590   Channels. *Braided Rivers*, 153–175. https://doi.org/10.1002/9781444304374.ch7

591   Chatanantavet, P., & Parker, G. (2008). Experimental study of bedrock channel alluviation under

592   varied sediment supply and hydraulic conditions. *Water Resources Research*, *44*(12), 1–

593   19. https://doi.org/10.1029/2007WR006581

594   De Vries M. (1965). Considerations about non-steady bed-load transport in open channels. *Proc.*

595   *11th Int. Congr. IAHR, Delft, the Netherlands, 3-8*.

596   Defina, A. (2003). Numerical experiments on bar growth. *Water Resources Research*, *39*(4), 1–

597   12. https://doi.org/10.1029/2002WR001455

598   Demeter, G. I., Sklar, L. S., & Davis, J. R. (2005). The influence of variable sediment supply and

599   bed roughness on the spatial distribution of incision in a laboratory bedrock channel.

600   *2005 Fall Meeting of the AGU*, 2004.

601   Dietrich, W. E. (1982). Settling velocity of natural particles. *Water Resources Research*, *18*(6),

602   1615–1626. https://doi.org/10.1029/WR018i006p01615

603   Duan, J. G., & Julien, P. Y. (2005). Numerical simulation of the inception of channel

604   meandering. *Earth Surface Processes and Landforms*, *30*(9), 1093–1110.

605   https://doi.org/10.1002/esp.1264

606   Engelund, F. (1977). *Hydraulic resistance for flow over dunes.*

607   Finnegan, N. J., Sklar, L. S., & Fuller, T. K. (2007). Interplay of sediment supply, river incision,

608   and channel morphology revealed by the transient evolution of an experimental bedrock

609   channel. *Journal of Geophysical Research: Earth Surface*, *112*(3), 1–17.

610   https://doi.org/10.1029/2006JF000569

611   Gasparini, N. M., Whipple, K. X., & Bras, R. L. (2007). Predictions of steady state and transient

612   landscape morphology using sediment-flux-dependent river incision models. *Journal of*

613   *Geophysical Research: Earth Surface*, *112*(3), 1–20.

614   https://doi.org/10.1029/2006JF000567

615   Grant, W. D., & Madsen, O. S. (1982). Movable bed roughness in unsteady oscillatory flow.

616   *Journal of Geophysical Research*, *87*(C1), 469–481.

617   https://doi.org/10.1029/JC087iC01p00469

618   Hartshorn, K., Hovius, N., Dade, W. B., & Slingerland, R. L. (2002). Climate-driven bedrock

619   incision in an active mountain belt. *Science*, *297*(5589), 2036–2038.

620   https://doi.org/10.1126/science.1075078

621   Hodge, R. A., & Hoey, T. B. (2012). Upscaling from grain-scale processes to alluviation in

622   bedrock channels using a cellular automaton model. *Journal of Geophysical Research:*

623   *Earth Surface*, *117*(F1), n/a-n/a. https://doi.org/10.1029/2011JF002145

624   Hodge, R. A., & Hoey, T. B. (2016a). A Froude-scaled model of a bedrock-alluvial channel

625   reach: 1. Hydraulics. *Journal of Geophysical Research: Earth Surface*, *121*(9), 1578–

626   1596. https://doi.org/10.1002/2015JF003706

627   Hodge, R. A., & Hoey, T. B. (2016b). A Froude-scaled model of a bedrock-alluvial channel

628   reach: 2. Sediment cover. *Journal of Geophysical Research: Earth Surface*, *121*(9),

629   1597–1618. https://doi.org/10.1002/2015JF003709

630   Howard, A. D. (1980). Thresholds in river regimes. In *Thresholds in Geomorphology* (pp. 227–

631   258).

632   Howard, A. D. (1987). Modelling Fluvial Systems: Rock-, Gravel-, and Sand-bed Channels. In

633   *River Channels: Environment and Process* (pp. 69–94).

634   Howard, A. D. (1998). Long profile development of bedrock channels: Interaction of weathering,

635   mass wasting, bed erosion, and sediment transport. In K. J. Tinkler & E. E. Wohl (Eds.),

636   *Rivers Over Rock: Fluvial Processes in Bedrock Channels* (Volume 107, pp. 297–319).

637   https://doi.org/10.1029/GM107p0297

638   Howard, A. D., Dietrich, W. E., & Seidl, M. A. (1994). Modeling fluvial erosion on regional to

639   continental scales. *Journal of Geophysical Research: Solid Earth*, *99*(B7), 13971–13986.

640   https://doi.org/10.1029/94JB00744

641   Inoue, T., Iwasaki, T., Parker, G., Shimizu, Y., Izumi, N., Stark, C. P., & Funaki, J. (2016).

642   Numerical Simulation of Effects of Sediment Supply on Bedrock Channel Morphology.

643   *Journal of Hydraulic Engineering*, 04016014. https://doi.org/10.1061/(ASCE)HY.1943-

644   7900.0001124

645   Inoue, T., Izumi, N., Shimizu, Y., & Parker, G. (2014). Interaction among alluvial cover, bed

646   roughness, and incision rate in purely bedrock and alluvial-bedrock channel. *Journal of*

647   *Geophysical Research: Earth Surface*, *119*(10), 2123–2146.

648   https://doi.org/10.1002/2014JF003133

649 Izumi, N., Yokokawa, M., & Parker, G. (2017). Incisional cyclic steps of permanent form in

650   mixed bedrock-alluvial rivers. *Journal of Geophysical Research: Earth Surface*, *122*(1),

651   130–152. https://doi.org/10.1002/2016JF003847

652 Knighton, D. (2014). *Fluvial Forms and Processes*. Routledge.

653   https://doi.org/10.4324/9780203784662

654 Lamb, M. P., Finnegan, N. J., Scheingross, J. S., & Sklar, L. S. (2015). New insights into the

655   mechanics of fluvial bedrock erosion through flume experiments and theory.

656   *Geomorphology*, *244*, 33–55. https://doi.org/10.1016/j.geomorph.2015.03.003

657 Lanzoni, S. (2000). Experiments on bar formation in a straight flume: 1. Uniform sediment.

658   *Water Resources Research*, *36*(11), 3337–3349. https://doi.org/10.1029/2000WR900160

659 Luu, L. X., Egashira, S., & Takebayashi, H. (2004). Investigation of Tan Chau Reach In Lower

660   Mekong Using Field Data And Numerical Simulation. *PROCEEDINGS OF*

661   *HYDRAULIC ENGINEERING*, *48*(5), 1057–1062. https://doi.org/10.2208/prohe.48.1057

662 Maddux, T. B., McLean, S. R., & Nelson, J. M. (2003). Turbulent flow over three-dimensional

663   dunes: 2. Fluid and bed stresses. *Journal of Geophysical Research: Earth Surface*,

664   *108*(F1), n/a-n/a. https://doi.org/10.1029/2003jf000018

665 Maddux, T. B., Nelson, J. M., & McLean, S. R. (2003). Turbulent flow over three-dimensional

666   dunes: 1. Free surface and flow response. *Journal of Geophysical Research: Earth*

667   *Surface*, *108*(F1), n/a-n/a. https://doi.org/10.1029/2003JF000017

668 Mendoza, A., Abad, J. D., Langendoen, E. J., Wang, D., Tassi, P., & Abderrezzak, K. E. K.

669   (2017). Effect of Sediment Transport Boundary Conditions on the Numerical Modeling

670   of Bed Morphodynamics. *Journal of Hydraulic Engineering*, *143*(4), 04016099.

671   https://doi.org/10.1061/(ASCE)HY.1943-7900.0001208

672   Meyer-Peter, E., & Müller, R. (1948). Formulas for Bed-Load Transport. *Proceedings of the 2nd*

673   *Meeting of the International Association of Hydraulic Research*, 39–64.

674   https://doi.org/1948-06-07

675   Mishra, J., & Inoue, T. (2020). Alluvial cover on bedrock channels: applicability of existing

676   models. *Earth Surface Dynamics*, *8*(3), 695–716. https://doi.org/10.5194/esurf-8-695-

677   2020

678   Murray, A. B., & Paola, C. (1997). Properties of a cellular braided-stream model. *Earth Surface*

679   *Processes and Landforms*, *22*(11), 1001–1025. https://doi.org/10.1002/(SICI)1096-

680   9837(199711)22:11<1001::AID-ESP798>3.0.CO;2-O

681   Nelson, J. M., Bennett, J. P., & Wiele, S. M. (2003). Flow and sediment-transport modeling.

682   *Tools in Fluvial Geomorphology*. https://doi.org/10.1002/0470868333.ch18

683   Nelson, J. M., & Smith, J. D. (1989). Mechanics of flow over ripples and dunes. *Journal of*

684   *Geophysical Research*, *94*(C6), 8146. https://doi.org/10.1029/JC094iC06p08146

685   Nelson, P. A., Bolla Pittaluga, M., & Seminara, G. (2014). Finite amplitude bars in mixed

686   bedrock-alluvial channels. *Journal of Geophysical Research: Earth Surface*, *119*(3), 566–

687   587. https://doi.org/10.1002/2013JF002957

688   Nelson, P. A., McDonald, R. R., Nelson, J. M., & Dietrich, W. E. (2015a). Coevolution of bed

689   surface patchiness and channel morphology: 1. Mechanisms of forced patch formation.

690   *Journal of Geophysical Research F: Earth Surface*, *120*(9), 1687–1707.

691   https://doi.org/10.1002/2014JF003428

692   Nelson, P. A., McDonald, R. R., Nelson, J. M., & Dietrich, W. E. (2015b). Coevolution of bed

693   surface patchiness and channel morphology: 2. Numerical experiments. *Journal of*

694   *Geophysical Research F: Earth Surface*, *120*(9), 1708–1723.

695   https://doi.org/10.1002/2014JF003429

696   Nelson, P. A., & Seminara, G. (2012). A theoretical framework for the morphodynamics of

697   bedrock channels. *Geophysical Research Letters*, *39*(6), 1–7.

698   https://doi.org/10.1029/2011GL050806

699   Nittrouer, J. A., Mohrig, D., Allison, M. A., & Peyret, A. P. B. (2011). The lowermost

700   Mississippi River: A mixed bedrock-alluvial channel. *Sedimentology*, *58*(7), 1914–1934.

701   https://doi.org/10.1111/j.1365-3091.2011.01245.x

702   Parker, G., & Klingeman, P. C. (1982). On why gravel bed streams are paved. *Water Resources*

703   *Research*, *18*(5), 1409–1423. https://doi.org/10.1029/WR018i005p01409

704   Parker, G., & Toro-Escobar, C. M. (2002). Equal mobility of gravel in streams: The remains of

705   the day. *Water Resources Research*, *38*(11), 46-1-46–48.

706   https://doi.org/10.1029/2001wr000669

707   Qian, H., Cao, Z., Liu, H., & Pender, G. (2017). Numerical modelling of alternate bar formation,

708   development and sediment sorting in straight channels. *Earth Surface Processes and*

709   *Landforms*, *42*(4), 555–574. https://doi.org/10.1002/esp.3988

710   Raudkivi, A. J. (1997). Ripples on Stream Bed. *Journal of Hydraulic Engineering*, *123*(1), 58–

711   64. https://doi.org/10.1061/(ASCE)0733-9429(1997)123:1(58)

712   Ribberink, J. S. (1987). Mathematical modelling of one-dimensional morphological changes in

713   rivers with non-uniform sediment. *Communications on Hydraulic & Geotechnical*

714   *Engineering - Delft University of Technology*, 87–2.

715 Schuurman, F., Marra, W. A., & Kleinhans, M. G. (2013). Physics-based modeling of large

716   braided sand-bed rivers: Bar pattern formation, dynamics, and sensitivity. *Journal of*

717   *Geophysical Research: Earth Surface*, *118*(4), 2509–2527.

718   https://doi.org/10.1002/2013JF002896

719 Seidl, M., & Dietrich, W. (1992). The problem of channel erosion into bedrock. *Catena*,

720   *23*(Supplement), 101–104.

721 Sklar, L., & Dietrich, W. (1998). River longitudinal profiles and bedrock incision models:

722   Stream power and the influence of sediment supply. In K. J. Tinkler & E. E. Wohl (Eds.),

723   *Rivers Over Rock: Fluvial Processes in Bedrock Channels* (Volume 107, pp. 237–260).

724   https://doi.org/10.1029/GM107p0237

725 Sklar, L., & Dietrich, W. (2001). Sediment and rock strength controls on river incision into

726   bedrock. *Geology*, *29*(12), 1087. https://doi.org/10.1130/0091-

727   7613(2001)029<1087:SARSCO>2.0.CO;2

728 Sklar, L., & Dietrich, W. (2004). A mechanistic model for river incision into bedrock by

729   saltating bed load. *Water Resources Research*, *40*(6), 1–21.

730   https://doi.org/10.1029/2003WR002496

731 Smith, J. D., & Mclean, S. R. (1984). A Model for Flow in Meandering Streams. *Water*

732   *Resources Research*, *20*(9), 1301–1315. https://doi.org/10.1029/WR020i009p01301

733 Smith, J. D., & McLean, S. R. (1977). Spatially averaged flow over a wavy surface. *Journal of*

734   *Geophysical Research*, *82*(12), 1735. https://doi.org/10.1029/JC082i012p01735

735 Soulsby, R. (1997). Dynamics of Marine Sands. In *Dynamics of Marine Sands*. Thomas Telford

736   Ltd. https://doi.org/10.1680/DOMS.25844

737   Stansby, P. (2003). A mixing-length model for shallow turbulent wakes. *Journal of Fluid*

738   *Mechanics*, *495*, 369–384. https://doi.org/10.1017/S0022112003006384

739   Struiksma, N. (1985). Prediction of 2-D bed topography in rivers. *Journal of Hydraulic*

740   *Engineering*, *111*(8), 1169–1182. https://doi.org/10.1061/(ASCE)0733-

741   9429(1985)111:8(1169)

742   Talmon, A. M., Struiksma, N., & Van Mierlo, M. C. L. M. (1995). Laboratory measurements of

743   the direction of sediment transport on transverse alluvial-bed slopes. *Journal of*

744   *Hydraulic Research*, *33*(4), 495–517. https://doi.org/10.1080/00221689509498657

745   Tinkler, K., & Wohl, E. (1998). A Primer on Bedrock Channels. In K. Tinkler & E. Wohl (Eds.),

746   *Rivers Over Rock: Fluvial Processes in Bedrock Channels* (Vol. 107, pp. 1–18).

747   Blackwell Publishing Ltd. https://doi.org/10.1029/GM107P0001

748   Toro, E. F. (2009). The HLL and HLLC Riemann Solvers. In *Riemann Solvers and Numerical*

749   *Methods for Fluid Dynamics* (pp. 315–344). Springer Berlin Heidelberg.

750   https://doi.org/10.1007/b79761_10

751   Turowski, J. M., Hovius, N., Meng-Long, H., Lague, D., & Men-Chiang, C. (2008). Distribution

752   of erosion across bedrock channels. *Earth Surface Processes and Landforms*, *33*(3), 353–

753   363. https://doi.org/10.1002/esp.1559

754   Turowski, J. M., Hovius, N., Wilson, A., & Horng, M. J. (2008). Hydraulic geometry, river

755   sediment and the definition of bedrock channels. *Geomorphology*, *99*(1–4), 26–38.

756   https://doi.org/10.1016/j.geomorph.2007.10.001

757   Turowski, J. M., Lague, D., & Hovius, N. (2007). Cover effect in bedrock abrasion: A new

758   derivation and its implications for the modeling of bedrock channel morphology. *Journal*

759   *of Geophysical Research: Earth Surface*, *112*(4), 1–16.

760   https://doi.org/10.1029/2006JF000697

761 Van der Meer, C., Mosselman, E., Sloff, K., Jager, B., Zolezzi, G., & Tubino, M. (2011).

762   Numerical simulations of upstream and downstream overdeepening. *River, Coastal and*

763   *Estuarine Morphodynamics*, *1967*, 1721–1729.

764 van Rijn, L. C. (1982). Equivalent Roughness of Alluvial Bed. *Journal of the Hydraulics*

765   *Division*, *108*(10), 1215–1218. https://doi.org/10.1061/JYCEAJ.0005917

766 van Rijn, L. C. (1984). Sediment Transport, Part II: Suspended Load Transport. *Journal of*

767   *Hydraulic Engineering*, *110*(11), 1613–1641. https://doi.org/10.1061/(ASCE)0733-

768   9429(1984)110:11(1613)

769 Vanoni, V. A., & Hwang, L.-S. (1967). Relation Between Bed Forms and Friction in Streams.

770   *Journal of the Hydraulics Division*, *93*(3), 121–144.

771   https://doi.org/10.1061/jyceaj.0001607

772 Vermeer, K. (1986). The ripple factor in sediment transport equations. *Rep. R657/M1314-V*.

773 Whipple, K. X. (2001). Fluvial Landscape Response Time: How Plausible Is Steady-State

774   Denudation? *American Journal of Science*, *301*(4–5), 313–325.

775   https://doi.org/10.2475/ajs.301.4-5.313

776 Whipple, K. X. (2004). Bedrock rivers and the geomorphology of active orogens. In *Annual*

777   *Review of Earth and Planetary Sciences* (Vol. 32, Issue 1, pp. 151–185).

778   https://doi.org/10.1146/annurev.earth.32.101802.120356

779 Whipple, K. X., & Tucker, G. E. (1999). Dynamics of the stream-power river incision model:

780   Implications for height limits of mountain ranges, landscape response timescales, and

781   research needs. *Journal of Geophysical Research: Solid Earth*, *104*(B8), 17661–17674.

782   https://doi.org/10.1029/1999JB900120

783   Whipple, K. X., & Tucker, G. E. (2002). Implications of sediment-flux-dependent river incision

784   models for landscape evolution. *Journal of Geophysical Research*, *107*(B2), 2039.

785   https://doi.org/10.1029/2000JB000044

786   Wiberg, P. L., & Nelson, J. M. (1992). Unidirectional flow over asymmetric and symmetric

787   ripples. *Journal of Geophysical Research*, *97*(C8), 12745.

788   https://doi.org/10.1029/92JC01228

789   Wiberg, P. L., & Rubin, D. M. (1989). Bed roughness produced by saltating sediment. *Journal of*

790   *Geophysical Research*, *94*(C4), 5011. https://doi.org/10.1029/JC094iC04p05011

791   Wiberg, P. L., & Smith, J. D. (1987). Calculations of the critical shear stress for motion of

792   uniform and heterogeneous sediments. *Water Resources Research*, *23*(8), 1471–1480.

793   https://doi.org/10.1029/WR023i008p01471

794   Wohl, E. E. (1993). Bedrock Channel Incision along Piccaninny Creek, Australia. *The Journal of*

795   *Geology*, *101*(6), 749–761. https://doi.org/10.1086/648272

796   Wu, F. C., Shao, Y. C., & Chen, Y. C. (2011). Quantifying the forcing effect of channel width

797   variations on free bars: Morphodynamic modeling based on characteristic dissipative

798   Galerkin scheme. *Journal of Geophysical Research: Earth Surface*, *116*(3), 1–20.

799   https://doi.org/10.1029/2010JF001941

800   Zhang, L., Parker, G., Stark, C. P., Inoue, T., Viparelli, E., Fu, X., & Izumi, N. (2015). Macro-

801   roughness model of bedrock-alluvial river morphodynamics. *Earth Surface Dynamics*,

802   *3*(1), 113–138. https://doi.org/10.5194/esurf-3-113-2015

803   Zhang, L, Iwasaki, T., Li, T., Fu, X., Wang, G., & Parker, G. (2019). Bedrock-alluvial streams

804   with knickpoint and plunge pool that migrate upstream with permanent form. *Scientific*

805   *Reports*, *9*(1), 1–9. https://doi.org/10.1038/s41598-019-42389-2

806   Zhang, L, Stark, C., Schumer, R., Kwang, J., Li, T., Fu, X., Wang, G., & Parker, G. (2018). The

807   Advective-Diffusive Morphodynamics of Mixed Bedrock-Alluvial Rivers Subjected to

808   Spatiotemporally Varying Sediment Supply. *Journal of Geophysical Research: Earth*

809   *Surface*, *123*(8), 1731–1755. https://doi.org/10.1029/2017JF004431